Inorganic Chemistry
Cite This: Inorg. Chem. XXXX, XXX, XXX−XXX
Article
pubs.acs.org/IC

Formation Mechanism, Structural, and Upconversion Properties of Alkaline Rare-Earth Fluoride Nanocrystals Doped With Yb^{3+}/Er^{3+} Ions

Tomasz Grzyb* and Dominika Przybylska

Department of Rare Earths, Faculty of Chemistry, Adam Mickiewicz University in Poznan, Umultowska 89b, 61-614 Poznan, Poland

Supporting Information

ABSTRACT: Ultrasmall (9−30 nm) Yb^{3+}/Er^{3+}-doped, upconverting alkaline rare-earth fluorides that are promising for future applications were synthesized by the microwave-assisted hydrothermal method. The formation mechanism was proposed, indicating the influence of the stability of metal ions complexes with ethylenediaminetetraacetic acid on the composition of the product and tendency to form M_2REF_7 ($M_{0.67}RE_{0.33}F_{2.33}$) cubic compounds in the M−RE−F systems. Their physicochemical properties (structure, morphology, and spectroscopic properties) are compared and discussed. The obtained nanoparticles exhibited emission of light in the visible spectra under excitation by 976 nm laser radiation. Excitation and emission spectra, luminescence decays, laser energy dependencies, and upconversion quantum yields were measured to determine the spectroscopic properties of prepared materials. The Yb^{3+}/Er^{3+} pair of ions used as dopants was responsible for an intense yellowish-green emission. The upconversion quantum yields determined for the first time for M_2REF_7-based materials were 0.0192 ± 0.001% and 0.0176 ± 0.001% for Sr_2LuF_7:Yb^{3+},Er^{3+} and Ba_2LuF_7:Yb^{3+},Er^{3+} respectively, the two best emitting samples. These results indicated the prepared materials are good and promising alternatives for the most studied $NaYF_4$:Yb^{3+},Er^{3+} nanoparticles.

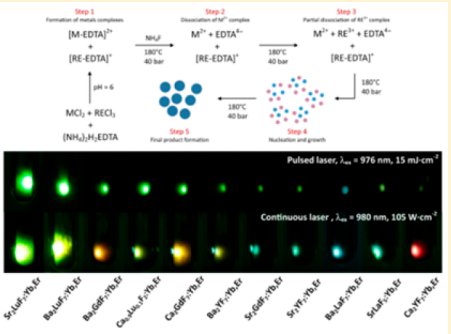

INTRODUCTION

In recent years, the properties of upconverting nanoparticles (UCNPs) have been investigated very intensively because of their potential applications. Particularly interesting are UCNPs based on lanthanide ions (Ln^{3+}).[1−3] Knowledge of the mechanisms responsible for the efficient upconversion process is increasing dynamically.[4−6] Furthermore, methods of nanoparticles (NPs) production are continuously developing as the demand for smaller and more advanced NPs is growing.[7,8]

Ln^{3+} ions feature narrow-band absorption and emission that are characteristic of these emitter ions, a large number of excited states, long luminescence lifetimes, large Stokes shift and upconversion (UC) phenomenon. The combination of these properties allows use of the materials doped with Ln^{3+} ions in solar cells, lasers and fiber amplifiers, persistent phosphors, and temperature/pressure sensors.[9−16] Inorganic nanomaterials doped with Ln^{3+} ions, excited under near-infrared radiation (NIR), can be applied in bioimaging, cancer treatment, or drug delivery.[17−20] The use of UCNPs for cell imaging ensures low autofluorescence and reduction of light scattering generated by tissue.[21−24] Moreover, UCNPs are known to cause less photodamage to cells and usually have low cytotoxicity.[25−27]

The morphology and composition of NPs are sometimes critical and often determine their applications. In nanomedicine, the important feature is the small average size of NPs, usually below 50 nm. Small NPs are noninvasive to cells and may be distributed in organism through blood vessels.[25,26] Another fundamental property of the described compounds is high photochemical stability and resistance to photobleaching. An additional advantage of inorganic NPs is also the fact that their surface can be very easily modified, e.g., by using silica, and further biologically functionalized.[28−32]

The most popular and commonly used inorganic host materials for UC are fluorides. They have low phonon energy, which reduces the possibility of the occurrence of nonradiative relaxation, and high chemical stability. Nanomaterials based on fluorides are characterized by a relatively high quantum yield (QY) of luminescence.[33−36] Nanocrystalline fluorides can be synthesized by several methods, of which the most common is the decomposition of product precursors (e.g., metal trifluoroacetates) in high-boiling solvents, such as oleic acid and octadecene.[7,37,38] Other methods are based on the precipitation reaction, also carried out under solvo- or hydrothermal conditions.[39−41]

Recently, the $NaYF_4$ matrix has been used most frequently in research concerning UC systems.[42,43] UCNPs based on this compound are small, with high emission quantum yields (see Table S2).[43−46] However, growing interest in the application of nanomaterials has created a need for new compounds with bright emissions and effective methods for their synthesis. Other fluorides, such as $M_xRE_yF_z$ systems (where M = Ca, Sr, Ba, and RE = Y, La, Gd, Lu) are relatively less studied. Only a few reports about $Ca_xRE_yF_z$ and $Sr_xRE_yF_z$ UCNPs are available.[47−49] Similar compounds, like $BaYF_5$ or $BaGdF_5$,

Received: February 22, 2018

DOI: 10.1021/acs.inorgchem.8b00484
Inorg. Chem. XXXX, XXX, XXX−XXX

have more often been the subject of studies revealing promising upconversion properties.[50,51] The current state of knowledge about M_2REF_7-type compounds indicates that several of the UC materials presented in this article, such as Ca_2YF_7, Ca_2GdF_7, and Ba_2LuF_7, have not been as yet subjects of literature reports. Other ones, such as Sr_2LuF_7, Ba_2YF_7, and Ba_2GdF_7, have been more studied, but the upconversion quantum yields (UCQY) in these systems have not been reported to date.[52−56]

Synthesis of nanocrystalline $M_xRE_yF_z$ fluorides is usually not an easy process because of the diversity of their stoichiometry and crystal structures.[57−59] Very often, the resulting products have more than one crystal phase. Fedorov et al. analyzed BaF_2−YF_3 systems proving a nonequilibrium character of these phases.[60] Therefore, there is not possible to obtain barium−yttrium fluorides with a specific composition, e.g., $BaYF_5$. Instead, these systems should be considered as $Ba_{1-x}RE_xF_{2+x}$ solid solutions.[60] Despite this, there are some articles using the $BaYF_5$ formula.[51,61−63] Although some of the mixed M^{2+} and RE^{3+} fluorides have been investigated in recent years, their UC properties have not been compared. What is more, there is a high degree of uncertainty regarding the product composition in published articles. Therefore, it is important to carefully examine the properties of obtained M_xREF_{2x+3} compounds and determine their real stoichiometry. Our studies show that M−RE−F systems are complex and require deep investigation. Synthesis of NPs based on the compounds mentioned above and analysis of their properties can expand knowledge of these and similar systems, and also enlarge the base of inorganic nanomaterials for UC applications.

■ EXPERIMENTAL SECTION

Materials. Rare earth oxides: Y_2O_3, La_2O_3, Gd_2O_3, Er_2O_3, Yb_2O_3, and Lu_2O_3 (99.99%, Stanford Materials, United States) were used as the source of RE^{3+} (and Ln^{3+}) ions. To obtain rare earth chloride solutions at a concentration of 1 or 0.5 M, the oxides were dissolved separately in hydrochloric acid (ultrapure, Sigma-Aldrich, 37%, Poland). Ammonium fluoride (98+%, Sigma-Aldrich, Poland) was used as the source of fluoride ions. Barium chloride dehydrate (Sigma-Aldrich, 99+%, Poland), calcium chloride dihydrate (Sigma-Aldrich, 99+%, Poland), strontium chloride hexahydrate (Sigma-Aldrich, 99+%, Poland), and ethylenediaminetetraacetic acid (EDTA) diammonium salt hydrate (Sigma-Aldrich, 97%, Poland) were used as received without further purification.

Synthesis. Nanoparticles showing UC based on M_2REF_7 matrices (where M = Ca, Sr, Ba, and RE = Y, La, Gd, Lu) doped with Yb^{3+} and Er^{3+} ions were synthesized using the microwave-assisted hydrothermal method (Magnum II, Ertec). To obtain M_2REF_7:Yb^{3+},Er^{3+} (theoretical concentrations were set to 18% and 2% mol), 6 mmol of EDTA diammonium salt hydrate was dissolved in 20 mL of water, in a beaker which was placed on a magnetic stirrer. This substance was used to prevent precipitation of the product before applying the hydrothermal conditions. Then, an aqueous solution of MCl_2 (containing 3 mmol of reactant) mixed earlier in a beaker with $RECl_3$ and $LnCl_3$ (Ln = Yb, Er; total amount 3 mmol) with a specified concentration and stoichiometric ratio (1:1 metal ions) was added to dissolved EDTA. $NH_{3(aq)}$ (30%) was added dropwise upon vigorous stirring to obtain a transparent solution until pH = 6 was reached. NH_4F was used in the synthesis as a source of fluoride ions: metal and fluoride ions were mixed in a 1:5 ratio. During preparation of the solution, the pH was monitored and maintained at 6 using $NH_{3(aq)}$. The transparent solution with total volume of 70 mL was transferred into a Teflon-lined autoclave (100 mL) and treated under hydrothermal conditions for 4 h at 180 °C and 40 bar, with microwave heating. Afterward, the obtained white precipitate was purified by centrifugation with water and ethanol several times. The final product was dried at 80 °C for 80 h.

Characterization. X-ray diffractograms (XRD) were recorded on a Bruker AXS D8 Advance diffractometer in the Bragg−Brentano geometry, with Cu $K_{\alpha 1}$ radiation, in the 2θ range from 6 to 60°. The reference data were taken from The International Centre for Diffraction Data (ICDD) database. Crystal cell volumes were calculated using the Maud 2.33 software.[64] The composition of the prepared materials was analyzed by inductively coupled plasma-optical emission spectrometer (Varian ICP-OES VISTA-MPX). Transmission-electron-microscopy (TEM) images were recorded on an FEI Tecnai G2 20 X-TWIN transmission electron microscope using an accelerating voltage of 200 kV.

The luminescence characteristics (excitation, emission spectra, luminescence decays, and power dependencies) of the prepared samples were measured on a Photon Technology International QuantaMaster 40 spectrofluorometer equipped with an Opotek Inc. Opolette 355LD UVDM tunable laser, with a repetition rate of 20 Hz and pulse length of 7 ns; a Hamamatsu R928 photomultiplier was used as a detector and a Thorlabs FEL900 optical filter was used.

The absolute upconversion quantum yield (UCQY) measurements usually involve the use of integrating sphere.[43,44,65−67] In our studies a barium sulfate-coated integrating sphere (80 mm diameter) from Photon Technology International was employed. The integrating sphere was mounted in a QuantaMaster 40 spectrofluorometer with the entry and output ports located at 90° to each other. A continuous Dragon Lasers DPSS 980 nm laser was used as the excitation source, coupled to a 200 μm optical fiber and collimator. A S305C Compact Thermal Power Sensor from Thorlabs was used to measure the power of the laser beam. As a detector, a Princeton Instruments PIXIS:256E Digital CCD Camera, equipped with an SP-2156 Imaging Spectrograph was applied, corrected for the instrumental response. All of the powder samples were held in a white Teflon cuvette with a quartz window, located in the center of the integrating sphere. Two filters, Thorlabs NENIR30B and NENIR40B, were used in order to measure the spectrum in the range covering the emission and excitation wavelengths (500−1050 nm) and to avoid saturation of the CCD camera. Measured spectra were corrected for the filters before the final calculations. For more details see Supporting Information.

Pictures of the samples were taken using a Canon EOS 550D camera under excitation by Opolette 355LD UVDM (~10 mJ·cm^{-2}) or a Dragon Lasers DPSS 980 nm laser (~20 W·cm^{-2}) and with Thorlabs FEL900 and FGS900-A optical filters (exposure time 2.5 s, f/4, ISO-1600).

■ RESULTS AND DISCUSSION

Structure and Morphology. The $M_xRE_yF_z$ fluorides are known to crystallize as cubic, orthorhombic, hexagonal, or monoclinic structures depending on the composition.[57,59,68−70] The synthesized compounds crystallized as disordered, fluorite-type, nonstoichiometric structures with a $M_{0.67}RE_{0.33}F_{2.33}$ composition per unit cell and $Fm\overline{3}m$ cubic space group.[57,71] According to Sorokin et al., these type of compounds crystallize as solid solutions which remain metastable at low temperature.[71] The article uses the M_2REF_7 formula containing the integer number of ions. Upon annealing, the fluorite structure may order with formation of tetragonal M_2REF_7 phase.[71] The diffraction peaks of tetragonal phase are similar to those of the pure cubic structure, $Fm\overline{3}m$; however, according to literature, the compounds obtained by solid-state reaction may show very weak additional superstructure reflections.[72] Also splitting of the main peaks of the fluorite-type lattice phase should be observed.[71] These minor peaks as well as splitting of XRD peaks were not observed in the materials prepared, which confirms the cubic structure. However, there are some articles incorrectly reporting M_2REF_7-type compounds as tetragonal

DOI: 10.1021/acs.inorgchem.8b00484
Inorg. Chem. XXXX, XXX, XXX−XXX

with similar XRD patterns to those presented in this article.[52,53,56,73]

The crystal phases of all samples have been identified, and the results are presented in Figure 1. The diffraction peaks are broad, which indicates the small size of the nanocrystals (Table 1). The obtained patterns were compared to the standard data for cubic $Sr_{0.68}Pr_{0.32}F_{2.32}$ (ICSD No. 190727). The comparison confirmed the single-phase structure of all the compounds. Depending on the ions forming the material, crystal cell volume (Table 1) changed in comparison to that for the reference compound, which resulted in a shift of the XRD peaks. Hence, when the host compound consists of Ba^{2+} (r = 1.35 Å), the calculated crystal cell volumes are the largest, and the shifts of the XRD peaks with respect those in the reference pattern are the highest. Analogously, the materials including Ca^{2+} ions with the ionic radius smaller than that of the M^{2+} metal ions used (r = 1.00 Å) had the smallest cell volumes from all products obtained. In addition, differences between ionic radii of RE^{3+} ions caused similar changes, although to a smaller degree as the differences were also lower: Y^{3+} (r = 0.9 Å), La^{3+} (r = 1.03 Å), Gd^{3+} (r = 0.94 Å), and Lu^{3+} (r = 0.86) (ionic radius for the coordination number, CN = 6). The size of nanocrystals, calculated from the Scherrer equation, was independent of the crystal cell volume.

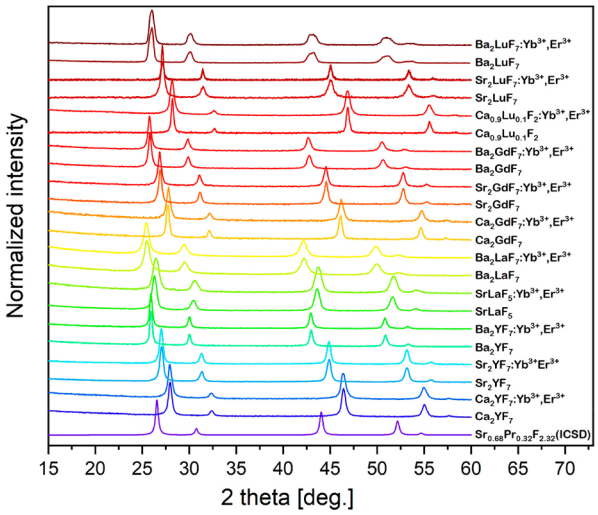

Figure 1. XRD patterns of the samples synthesized by hydrothermal method and the reference from the ICSD database (No. 190727).

ICP-OES analysis was performed to confirm the obtained stoichiometry, and the results are presented in Table 1. Figure 1 presents the XRD patterns of the obtained compounds along with sample labels according to their elemental composition. On the basis of the elemental analysis, three different types of structures were obtained: $MREF_5$ ($SrLaF_5$), M_2REF_7 (Ca_2YF_7, Sr_2YF_7, Ba_2YF_7, Ba_2LaF_7, Ca_2GdF_7, Sr_2GdF_7, Ba_2GdF_7, Sr_2LuF_7, Ba_2LuF_7, and $M_{1-x}RE_xF_{2+x}$ for a structure containing Ca^{2+} and Lu^{3+} ions with a very low content of lanthanide ions.

The complexity of the M−RE−F systems results from the high capacity of the CaF_2 fluorite-type structure for ion exchange. The M^{2+} ions can be easily replaced by RE^{3+} ions, which additionally are similar in ionic radius to those they replace. The charge imbalance created after replacement can be compensated by highly mobile F^- ions. Hence, from the ideal fluorite-type CaF_2 structure, other structures can be delivered, such as tetragonal-type distortion.[74] However, in nanocrystalline materials in which a high proportion of ions are localized

Table 1. Results of ICP-OES Analysis, the Stoichiometric Ratio between Alkaline Metal (Ca, Sr, Ba) and Rare Earth Ions, Crystal Cell Volumes, and Nanocrystal Sizes Calculated Using the Scherrer Equation

metal ion		concentration (% mol)							
M^{2+}	RE^{3+}	M^{2+}	RE^{3+}	Yb^{3+}	Er^{3+}	M^{2+}:RE^{3+} ratio	sample name	crystal cell volume (Å^3)	nanocrystal size (nm)
Ca^{2+}		70.0	30.0			2:0.9	Ca_2YF_7	170.38	16.4 ± 1.6
		74.2	24.6	1.0	0.2	2:0.7	Ca_2YF_7:3.9%Yb^{3+},0.6%Er^{3+}	169.47	13.7 ± 1.6
Sr^{2+}	Y^{3+}	66.6	33.4			2:1.0	Sr_2YF_7	187.40	16.1 ± 0.6
		64.1	33.6	2.0	0.3	2:1.1	Sr_2YF_7:5.6%Yb^{3+},0.9%Er^{3+}	186.65	16.3 ± 0.8
Ba^{2+}		66.4	33.6			2:1.0	Ba_2YF_7	210.78	19.7 ± 1.7
		69.3	28.9	1.6	0.3	2:0.9	Ba_2YF_7:5.1%Yb^{3+},0.9%Er^{3+}	211.15	19.7 ± 1.8
Ca^{2+}									
Sr^{2+}		52.6	47.4			2:1.8	$SrLaF_5$	202.35	13.2 ± 1.2
	La^{3+}	55.3	44.2	0.4	0.1	2:1.6	$SrLaF_5$:0.8%Yb^{3+},0.2%Er^{3+}	200.40	10.7 ± 1.0
Ba^{2+}		67.1	32.9			2:1.0	Ba_2LaF_7	221.78	9.4 ± 0.6
		63.3	36.2	0.4	0.1	2:1.2	Ba_2LaF_7:1.1%Yb^{3+},0.2%Er^{3+}	223.21	10.3 ± 0.9
Ca^{2+}		67.0	33.0			2:1.0	Ca_2GdF_7	172.87	20.8 ± 4.4
		73.3	25.6	1.0	0.2	2:0.7	Ca_2GdF_7:3.7%Yb^{3+},0.7%Er^{3+}	171.90	15.5 ± 1.1
Sr^{2+}	Gd^{3+}	71.7	28.3			2:0.8	Sr_2GdF_7	189.90	20.8 ± 6.0
		60.4	37.1	2.2	0.3	2:1.3	Sr_2GdF_7:5.5%Yb^{3+},0.9%Er^{3+}	190.90	18.0 ± 2.9
Ba^{2+}		74.0	26.0			2:0.7	Ba_2GdF_7	213.72	14.7 ± 1.7
		72.6	25.1	2.1	0.3	2:0.8	Ba_2GdF_7:7.5%Yb^{3+},1.1%Er^{3+}	214.77	15.4 ± 1.9
Ca^{2+}		89.6	10.4			2:0.2	$Ca_{0.9}Lu_{0.1}F_2$	164.57	20.0 ± 2.2
		86.4	9.6	3.5	0.5	2:0.3	$Ca_{0.9}Lu_{0.1}F_2$:3.5%Yb^{3+},0.5%Er^{3+}	164.96	14.6 ± 1.7
Sr^{2+}	Lu^{3+}	72.3	27.7			2:0.8	Sr_2LuF_7	185.78	12.9 ± 1.6
		67.8	25.1	6.2	1.0	2:1.0	Sr_2LuF_7:19.3%Yb^{3+},3.0%Er^{3+}	184.17	20.5 ± 1.9
Ba^{2+}		66.4	33.6			2:1.0	Ba_2LuF_7	210.16	10.6 ± 2.6
		66.1	25.1	7.7	1.1	2:1.0	Ba_2LuF_7:22.8%Yb^{3+},3.1%Er^{3+}	208.77	9.8 ± 2.6
		ICSD No. 190727					$Sr_{0.68}Pr_{0.32}F_{2.32}$	196.53	

DOI: 10.1021/acs.inorgchem.8b00484
Inorg. Chem. XXXX, XXX, XXX−XXX

on the surface (~20% in nanocrystals with size around 8 nm),[75] where the crystal structure is highly distorted and XRD peaks are wide, the boundary between cubic and tetragonal structure may be not clear.

The results of ICP-OES analysis typically indicated different composition of products and lower dopant concentrations than expected from stoichiometric calculations. Most of the products were obtained with M^{2+} to RE^{3+} molar ratios of around 2:1, despite the fact that MCl_2 and $RECl_3$ chlorides were added to the solution at the 1:1 molar ratio. Also the ratios of RE^{3+} ions forming host (Y^{3+}, La^{3+}, Gd^{3+}, or Lu^{3+}) to those used as dopants (Yb^{3+} and Er^{3+}) was not as expected from the concentrations of the reagents. The data presented in Table 1 show that the highest percentage amount of Yb^{3+} and Er^{3+} ions was found in the Ba_2LuF_7-based sample (22.8% and 3.04%, respectively). The lowest efficiency of doping was observed for $SrLaF_7$:Yb^{3+},Er^{3+} sample in which the dopant concentrations were 0.8% of Yb^{3+} and 0.2% of Er^{3+} ions.

As the reaction conditions and reagent compositions were the same for each synthesis, the final product stoichiometry and composition were determined by other factors. The differences in ionic radii between metal ions,[76] solubilities of metal fluorides,[77,78] and, the most important factor, stability of the complexes with EDTA are known to influence the properties of the materials obtained (see Table S1 in Supporting Information for appropriate data).[79] The proposed product formation mechanism is presented in Figure 2. Alkaline metals, M^{2+}, form

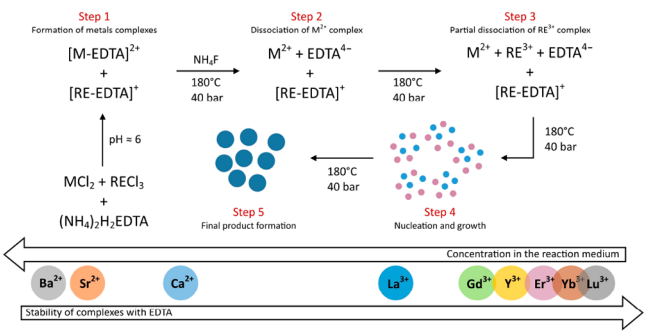

Figure 2. Proposition of mechanism of nanocrystal growth in hydrothermal conditions.

complexes with EDTA that are less stable than the complexes of RE^{3+} ions. An equilibrium between $[M\text{-}EDTA]^{2+}$, $[RE\text{-}EDTA]^{+}$, M^{2+}, RE^{3+}, and $EDTA^{4+}$ individuals is established after mixing all of the reagents. The RE^{3+} ions are in larger fraction complexed in $[RE\text{-}EDTA]^{+}$ than M^{2+} in $[M\text{-}EDTA]^{2+}$; therefore, the ratio between these ions is higher than expected. Additionally, after the reaction starts, $[M\text{-}EDTA]^{2+}$ complexes first dissociate (Step 2 in the mechanism) as they are less stable and as the result of EDTA decomposition.[80] Afterward, $[RE\text{-}EDTA]^{+}$ begins to dissociate, which explains why the concentration of RE^{3+} ions in the prepared materials is much lower than expected from the amounts of reagent salts added. After these two stages, the equilibrium between M^{2+}, RE^{3+}, and their complexes is established, and precipitation of the products begins (Step 4). The final step is nucleation followed by growth of nanoparticles (Step 5). This simplified mechanism is the only proposition not verified experimentally.

The proposed mechanism explains why most of the synthesized materials contained lower concentrations of Yb^{3+} and Er^{3+} dopants than expected (20% of Yb^{3+} and 2% of Er^{3+} ions) and why the fraction of precipitated Er^{3+} ions is always larger than that of Yb^{3+} ions (Table 1). The dopant ions precipitate, the last one during the reaction, first Er^{3+} and next Yb^{3+} ions, except for syntheses of NPs containing Lu^{3+} ions. This also explains the difference between Sr_2LuF_7- or Ba_2LuF_7-based materials and the rest of products.

In the group of synthesized materials, three exceptions were observed: in Ca^{2+}- and La^{3+}-containing mixtures, the product was not formed in the applied conditions; Sr^{2+} and La^{3+} ions precipitated as a $SrLaF_5$ compound; Ca^{2+} and Lu^{3+} formed a $Ca_{0.9}Lu_{0.1}F_2$ compound. The explanation of these results is unclear. It is worth noting that the difference between the ionic radii of Ca^{2+} and La^{3+} is the smallest of the all used metal ions as well as the difference in stability constant of EDTA complexes. In addition, the differences in the size of M^{2+} and RE^{3+} ions in the remaining two cases are one of the smallest. This may be associated with the tendency to form the structure closest to cubic CaF_2.

In our opinion, the information mentioned above is critical in designing the properties of fluoride nanocrystals and planning their syntheses. A similar mechanism can be extended to systems containing other chelating agents, such as citric acid or polyethylene glycol.

Morphology of the products was determined by analyzing XRD patterns and TEM images. The characteristics of the XRD patterns indicate the nanocrystallinity of the products. Average nanocrystal sizes, calculated using the Scherrer equation,[81] vary in the range 9−21 nm and are displayed in Table 1. The TEM images together with size distribution histograms are presented in Figure 3. They show a very similar, quasi-spherical shape of the nanocrystals as well as their tendency to agglomerate. However, some single nanocrystals can still be observed, proving that they are not strongly connected. The Ba_2LaF_7:Yb^{3+},Er^{3+} sample (Figure 3f) presented the smallest average particle size, estimated at approximately 9 nm, but the nanocrystal sizes of the other products were also small. The sample was composed of Ba_2LaF_7 nanocrystals making small clusters of several nanocrystals. Such behavior was not observed in other materials. The determined nanocrystal dimensions are comparable with those calculated from the Scherrer equation except for Ba_2YF_7:Yb^{3+},Er^{3+}. All nanocrystals exhibited a high degree of crystallinity.

Spectroscopic Properties. Upconversion properties were studied under excitation by a pulsed laser (λ_{ex} = 976 nm). Emission and excitation spectra are presented in Figure 4. Luminescence decays were also recorded for each transition band as well as the dependencies of the emission intensity on laser energy were obtained. The calculated emission lifetimes and the number of photons involved in the upconversion process are presented in Table 2. Experimental data (luminescence decays and dependencies of emission intensities on laser energy) are presented in the Supporting Information (Figures S3 and S4).

Figure 4 shows that the spectra of all samples show similar emission and excitation peaks with quite different intensities. The highest emission intensities were recorded for Sr_2LuF_7:Yb^{3+},Er^{3+} and Ba_2LuF_7:Yb^{3+},Er^{3+} samples. Also the emission intensity of Ba_2GdF_7:Yb^{3+},Er^{3+} was relatively high. The other materials showed low emission or their emission was even almost quenched, like, e.g., for Ca_2YF_7:Yb^{3+},Er^{3+}.

The excitation spectra observed in Figure 4 show a narrow band with the maximum at 976 nm, characteristic of the $^2F_{7/2} \rightarrow {}^2F_{5/2}$ transition of Yb^{3+} ions. These ions participate in the

DOI: 10.1021/acs.inorgchem.8b00484
Inorg. Chem. XXXX, XXX, XXX−XXX

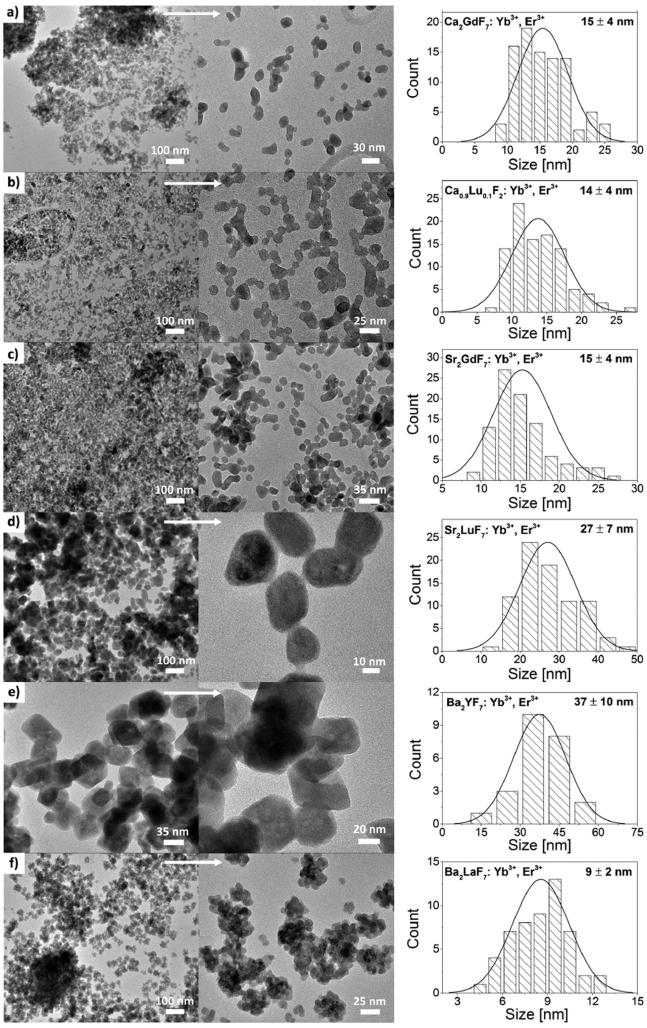

Figure 3. TEM images and nanocrystal size distributions of hydrothermally synthesized samples: (a) Ca_2GdF_7:Yb^{3+},Er^{3+}, (b) $Ca_{0.9}Lu_{0.1}F_2$:Yb^{3+},Er^{3+}, (c) Sr_2GdF_7:Yb^{3+},Er^{3+}, (d) Sr_2LuF_7:Yb^{3+}, Er^{3+}, (e) Ba_2YF_7:Yb^{3+},Er^{3+}, (f) Ba_2LaF_7:Yb^{3+}, Er^{3+}.

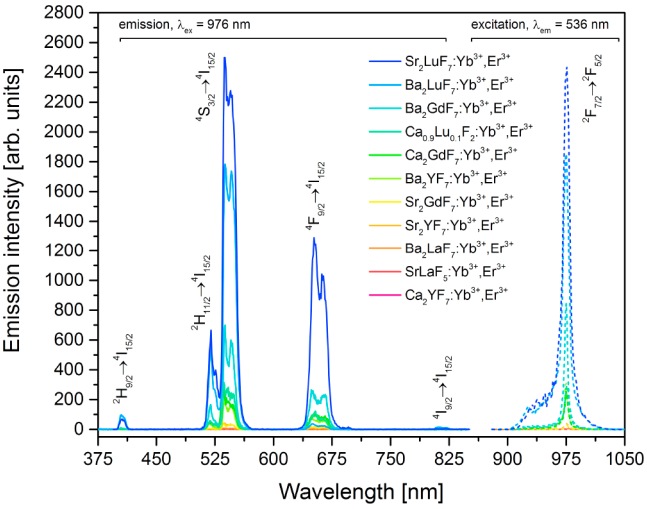

Figure 4. Upconversion luminescence (solid line) and excitation spectra of synthesized materials under pulsed excitation source (at 15 mJ·cm^{-2}).

energy transfer process (as sensitizers) to Er^{3+} ions, which results in photon upconversion.

The intensity of UC is connected with the concentration of Yb^{3+} ions. The samples in which the Yb^{3+} ion concentration is high also show intense emission, which may be expected as Yb^{3+} ions absorb exciting radiation. Analysis of the sample composition is crucial for the appropriate interpretation of spectroscopic results. The presented results indicate that preparation of a series of samples, keeping the same conditions in the synthesis, does not necessarily lead to the desired composition of each product.

In the emission spectra, the $^4S_{3/2} \rightarrow {}^4I_{15/2}$ transition (with a maximum at 536 nm) was observed as the most intense for all samples. Therefore, the color of the samples luminescence was green. The ratio between the intensities of transitions for the obtained nanopowders was very similar (see Figure S2). Four characteristic transitions of Er^{3+} ions: $^2H_{9/2} \rightarrow {}^4I_{15/2}$ (~406 nm), $^2H_{11/2} \rightarrow {}^4I_{15/2}$ (~520 nm), $^4S_{3/2} \rightarrow {}^4I_{15/2}$ (~540 nm), and $^4F_{9/2} \rightarrow {}^4I_{15/2}$ (~650 nm) were recorded only for some of the materials obtained: Sr_2LuF_7:Yb^{3+},Er^{3+}, Ba_2LuF_7:Yb^{3+},Er^{3+}, Ba_2GdF_7:Yb^{3+},Er^{3+}, $Ca_{0.9}Lu_{0.1}F_2$:Yb^{3+},Er^{3+}, and Ca_2GdF_7:Yb^{3+},Er^{3+}, which is related to the tendency of the $^2H_{9/2} \rightarrow {}^4I_{15/2}$ level to be quenched by a cross-relaxation process, or a noneffective, multiphonon de-excitation process.[82]

The upconversion quantum yields determined for the best emitting samples are presented in Figure 5. The calculated values were the highest for Sr_2LuF_7:Yb^{3+},Er^{3+} and Ba_2LuF_7:Yb^{3+},Er^{3+} the two best emitting samples (see also Table S2 and Figure 4). In these samples a saturation effect was observed, visible as a plateau-like region at higher power densities. The observed saturation may be explained by excitation trapping into intermediate state involved in UC mechanism. For Er^{3+} it is long-lived (bottleneck) $^4I_{13/2}$ excited state being unavailable for further excitation transfer at higher power densities.[10,83]

UCQYs are rarely published owing to the difficulties in their determination.[36,43,66,83−89] The obtained values are usually low, in comparison to those for downshifting phosphors. The highest published values do not exceed several percent, and they were determined only for the core/shell samples, prepared by the thermal decomposition method.[43,89,90] UCQY for a sample prepared by the hydrothermal method had been reported previously only once by Balabhadra et al.[66]

The most often studied $NaYF_4$:Yb^{3+},Er^{3+} nanoparticles, which showed one of the brightest emissions, revealed UCQY from 0.0022% to 0.32% under 980 nm laser irradiation, depending on the concentration of dopant ions, synthesis procedure, and particle size.[36,44,65,67,90] Comparison of UCQYs determined for samples doped with Yb^{3+} and Er^{3+} presented in Supporting Information (Table S2) shows that Sr_2LuF_7 and Ba_2LuF_7-based samples are capable of efficient emission, in some cases with higher quantum yield than for the most studied and best known $NaYF_4$:Yb^{3+},Er^{3+} nanoparticles. It should be emphasized that the materials prepared by us were obtained by the hydrothermal method based on water solution, in contrast to most of the other reports. UCQY values measured in nonwater solutions are usually higher.[46] Also reported power densities, used for UCQYs measurements, were usually higher than applied in this article.

Because of the nonlinear nature of UC, the QYs of this process are strongly dependent on the excitation density.[12,66,46,91] Furthermore, properties such as laser beam shape can also influence UCQYs.[43] Therefore, UC properties

DOI: 10.1021/acs.inorgchem.8b00484
Inorg. Chem. XXXX, XXX, XXX−XXX

Table 2. Emission Lifetimes Calculated on the Basis of Luminescence Decays and the Number of Photons Determined from Dependencies of Luminescence Intensity on Laser Energy[a]

sample name	emission lifetimes (μs)				number of photons			
	$^2H_{9/2} \rightarrow {}^4I_{15/2}$	$^2H_{11/2} \rightarrow {}^4I_{15/2}$	$^4S_{3/2} \rightarrow {}^4I_{15/2}$	$^4F_{9/2} \rightarrow {}^4I_{15/2}$	$^2H_{11/2} \rightarrow {}^4I_{15/2}$	$^2H_{11/2} \rightarrow {}^4I_{15/2}$	$^4S_{3/2} \rightarrow {}^4I_{15/2}$	$^4F_{9/2} \rightarrow {}^4I_{15/2}$
Ca_2YF_7:3.9%Yb^{3+},0.6%Er^{3+}		7.5	8.4	10.9		1.6	1.6	
Sr_2YF_7:5.6%Yb^{3+},0.9%Er^{3+}		20.1	20.3	65.6		1.1	1.5	1.2
Ba_2YF_7:5.1%Yb^{3+},0.9%Er^{3+}	74.4	73.4	107.7	336.7		1.8	2.3	1.9
$SrLaF_5$:0.8%Yb^{3+},0.2%Er^{3+}		22.4	35.5	95.2		1.2	0.75	
Ba_2LaF_7:1.1%Yb^{3+},0.2%Er^{3+}		27.7	28.8	144.9		1.6	1.5	1.3
Ca_2GdF_7:3.7%Yb^{3+},0.7%Er^{3+}	142.7	285.5	271.5	521.2	1.6	1.5	1.8	1.6
Sr_2GdF_7:5.5%Yb^{3+},0.9%Er^{3+}		18.1	19.9	48.1		1.1	1.5	1.4
Ba_2GdF_7:7.5%Yb^{3+},1.1%Er^{3+}	80.1	104.1	108.9	334.0	1.1	1.9	1.8	1.8
$Ca_{0.9}Lu_{0.1}F_2$:3.5%Yb^{3+},0.5% Er^{3+}	20.4	28.3	27.2	61.7	1.5	1.3	1.6	1.4
Sr_2LuF_7:19.3%Yb^{3+},3.0%Er^{3+}	65.6	103.2	106.9	225.2	2.5	1.5	1.6	1.7
Ba_2LuF_7:22.8%Yb^{3+},3.1%Er^{3+}	63.5	91.1	93.2	202.4		1.8	1.9	1.9

[a]Experimental data in Supporting Information, Figures S3 and S4.

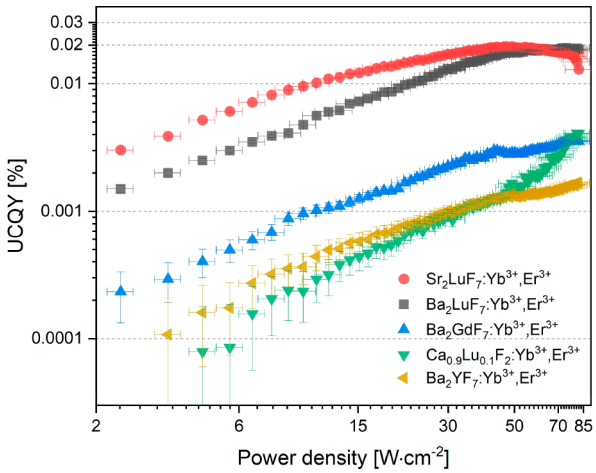

Figure 5. Upconversion quantum yields calculated for the best emitting samples.

are sensitive to instrumentation, which makes it difficult to compare properties of the same materials in different setups.[90]

The determined UCQYs were lower than for the best-known emitters. However, the emissions QY of Sr_2LuF_7:Yb^{3+},Er^{3+} and Ba_2Lu_7:Yb^{3+},Er^{3+} NPs are still at a satisfactory level, comparable with some of the reports for $NaREF_4$-type materials. This makes the obtained materials look promising for upconversion applications. Moreover, the M_2REF_7-type materials seem to be excellent candidates for synthesis by the thermal decomposition method.

The small difference in UCQY values between the two the best emitting materials results from different nanocrystals size, which are smaller in Ba_2Lu_7:Yb^{3+},Er^{3+} (see Table 1). The relatively low QY values of the remaining M^{2+}-RE^{3+} systems resulted from the low dopant concentrations. Also the synthesis method used, which requires the presence of water, may be responsible for low UCQY as the −OH oscillators quench the higher excited states of Ln^{3+} ions.[92] Other factors affecting UCQY are nonradiative processes between Ln^{3+} dopants, such as cross-relaxation and down-shifting emission of Yb^{3+} and Er^{3+} ions (above 1000 nm).[90] The dependence of QYs on the type of host used was similar as that presented in Figure 4.

The upconversion properties of the prepared materials were highly dependent on the excitation source, as shown in Figure 6. The pulsed excitation results mostly in a two-photon process (Table 2 and Figure S4), populating green- and red-emitting

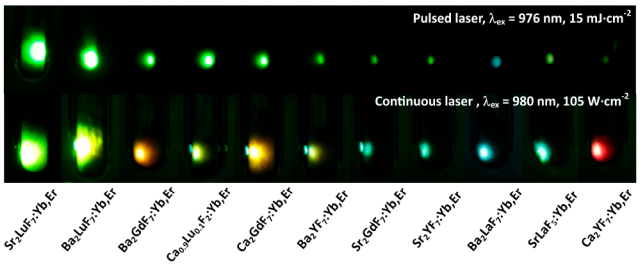

Figure 6. Upconversion luminescence images under NIR excitation (pulsed and continuous lasers).

Er^{3+} energy levels similarly, whereas continuous laser excitation may lead to a saturation effect, which was most noticeable for the green emission band at higher power densities.[43]

Luminescence decays measured for the obtained samples were used for calculation of luminescence lifetimes and are collected in Table 2 (for emission decays see Figure S3). From among all obtained matrices doped with Yb^{3+}/Er^{3+} ions, the longest emission was found for Ca_2GdF_7 (between 142.7 and 521.2 μs, depending on the transition band). Long lifetimes were also calculated for Ba_2YF_7 (74.4−336.7 μs) and Ba_2GdF_7-based materials (80.1−334.0 μs). The shortest (7.5−10.9 μs) emission was recorded for Ca_2YF_7:Yb^{3+},Er^{3+}, which may be connected to the very low content of dopant ions in this matrix. It is worth mentioning that for samples Sr_2LuF_7:Yb^{3+},Er^{3+} and Ba_2LuF_7:Yb^{3+},Er^{3+}, which exhibited the strongest emission of light from all samples, the lifetimes were relatively short (Sr_2LuF_7:Yb^{3+},Er^{3+} τ = 225.25 μs, Ba_2LuF_7: Yb^{3+},Er^{3+} τ = 202.41 μs for the $^4F_{9/2} \rightarrow {}^4I_{15/2}$ transition). The observed spectroscopic properties lead us to assume that the differences between samples are not only a result of their composition but also other factors. The EDTA adsorbed during the synthesis as well as the inhomogeneous distribution of dopant ions may also influence the upconversion process and luminescence decays.[93] This effect is especially visible in host materials in which alkaline M^{2+} ions are replaced by rare earth ions, RE^{3+}, requiring different charge compensation.

For all samples, the longest decay times were measured for the $^4F_{9/2} \rightarrow {}^4I_{15/2}$ transition. It may be caused by the necessity

DOI: 10.1021/acs.inorgchem.8b00484
Inorg. Chem. XXXX, XXX, XXX−XXX

of the cross-relaxation process preceding the feeding of the $^4F_{9/2}$ excited state or even a different excitation mechanism.[6] According to Xiang et al.,[94,95] if the decay time of the transition $^4F_{9/2} \rightarrow {}^4I_{15/2}$ is almost twice as long (or even more) than the $^4S_{3/2} \rightarrow {}^4I_{15/2}$ transition, the excitation to the $^4F_{9/2}$ level may occur from the $^4I_{13/2}$ excited state, which is directly populated by energy transfer from Yb^{3+} ions: $^4I_{13/2}$ (Er^{3+}) + $^2F_{5/2}$ (Yb^{3+}) to $^4F_{9/2}$ (Er^{3+}) + $^2F_{7/2}$ (Yb^{3+}). The long rise time for samples that exhibited good emission (Yb^{3+}- and Er^{3+}-doped: Ca_2GdF_7, $Ca_{0.9}Lu_{0.1}F_2$, Sr_2GdF_7, Sr_2LuF_7, Ba_2YF_7, Ba_2GdF_7, Ba_2LuF_7 hosts) can also be explained by this mechanism. If the excitation pathway occurs by multiphonon relaxation from $^2H_{11/2}$ to $^4F_{9/2}$, emission lifetime related to $^4F_{9/2} \rightarrow {}^4I_{15/2}$ transition should be similar to $^4S_{3/2} \rightarrow {}^4I_{15/2}$, which is true only for Ca_2YF_7 sample.

Dependencies of the luminescence intensity on the laser energy were also measured to better understand the mechanism of the UC process. They are presented in Supporting Information, Figure S4. At low power densities, the number of photons involved in the upconversion phenomena is equal to the slope coefficient in linear regressions obtained from excitation power dependencies. The determined numbers of photons involved in the upconversion mechanism are collected in Table 2.

The numbers of photons determined from the experimental data suggest that at least three photons are required to excite Er^{3+} ions to the $^2H_{9/2}$ level, and two photons to achieve $^2H_{11/2}$, $^4S_{3/2}$, and $^4F_{9/2}$ excited states. The schematic energy diagram presented in Figure 7 describes the proposed energy transfer

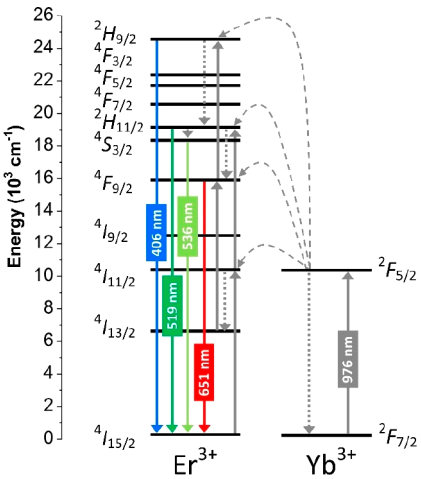

Figure 7. Schematic energy levels diagram for Yb^{3+} and Er^{3+} ion-doped samples.

processes occurring in the obtained materials. The $^4H_{9/2} \rightarrow {}^4I_{15/2}$ transition was recorded only for four obtained samples, but, unfortunately, the determined slope values were much lower than the theoretical ones. It is caused by nonradiative deactivation processes, such as cross-relaxation between Er^{3+} ions, and the saturation effect,[96−98] which appear at high laser energies. For Ba_2GdF_7, Ba_2YF_7, and Ca_2GdF_7-based materials, the calculated slope values are close to two for the $^2H_{11/2} \rightarrow {}^4I_{15/2}$, $^4S_{3/2} \rightarrow {}^4I_{15/2}$, and $^4F_{9/2} \rightarrow {}^4I_{15/2}$ transitions (preceded by two-photon excitation).[51] Interestingly, for the Ba_2YF_7:Yb^{3+},Er^{3+} sample, the $^4S_{3/2}$ excited state can also be achieved by three-photon absorption followed by relaxation from higher excited states.

On the basis of the obtained values of the slopes, which are greater than 1, it can be concluded that for the other matrices a two-photon process also occurred to excite Er^{3+} ions into their $^2H_{11/2}$, $^4S_{3/2}$, and $^4F_{9/2}$ levels. For the $SrLaF_5$ sample, only two transitions were measured: $^2H_{11/2} \rightarrow {}^4I_{15/2}$ and $^4S_{3/2} \rightarrow {}^4I_{15/2}$, for which the slope values were 1.22 and 0.75. This confirmed the occurrence of highly quenching processes in this sample and explained the very low emission.

Figure 7 shows the UC mechanism occurring in the obtained alkaline rare-earth fluoride matrices doped with Yb^{3+} and Er^{3+} ions. In these materials, the Yb^{3+} ions acted as sensitizers because of their simple energy level structure and high absorption coefficient in the NIR region. In turn, Er^{3+} ions acted as energy acceptors and luminescence activators. Yb^{3+} ions can be excited by radiation with a wavelength of around 976 nm, which provides a transition from the $^2F_{7/2}$ ground state to the $^2F_{5/2}$ excitation state, having similar energy to the $^4I_{11/2}$ excited state of Er^{3+} ions.[53] Therefore, energy can be relatively easily transferred to the neighboring Er^{3+} ions, raising them to the $^4I_{11/2}$ excited state level or, owing to the relaxation processes, to the $^4I_{13/2}$ excited state. Depending on the energy of Er^{3+} ions, two or three photons are required to observe green emission from the $^2H_{11/2}$ and $^4S_{3/2}$ levels. Er^{3+} ions, in their $^4I_{11/2}$ excited state, can absorb the second photon from Yb^{3+} ions, which promotes them to the $^2H_{11/2}$ excited state. Furthermore, neighboring Er^{3+} ions may act as sensitizers, transferring their energy to the Er^{3+} emitter.[97] From the $^2H_{11/2}$ excited state, green emission may occur, or relaxation to the $^4S_{3/2}$ excited state and finally green emission ($^4S_{3/2} \rightarrow {}^4I_{15/2}$ transition).

Excitation into the $^4F_{9/2}$ level of Er^{3+} ions may be realized in several different ways. The first possible pathway is a simple absorption of two photons as a result of energy transfer from Yb^{3+} ions, forming Er^{3+} ions in their $^2H_{11/2}$ excited state. Then, relaxation to the $^4F_{9/2}$ state takes place followed by red emission. However, at this point it needs to mentioned that the proposed pathway is not always realized. Other mechanisms may also be proposed to explain the origin of the red emission, including cross-relaxation between Er^{3+} ions, which depends on the Er^{3+} concentration.[6] Another possible pathway requires absorption of a photon from an excited Yb^{3+} ion to the $^4I_{11/2}$ level of the Er^{3+} ion, then relaxation to the $^4I_{13/2}$ state, from which the second absorbed photon results in the Er^{3+} ion in its $^4F_{9/2}$ excited state. Then the emission of red light can be observed.

Another explanation of the origin of the red emission and, in general, the UC mechanism at low Er^{3+} concentrations has been given by Berry et al.[6] In the proposed mechanism, they proved that red ($^4F_{9/2} \rightarrow {}^4I_{15/2}$) UC is preceded by a three-photon excitation process to $^4G/^2K$ states through the green emitting $^4S_{3/2}$ and $^2H_{11/2}$ states. Multiphonon relaxation from the Er^{3+} higher-excited states may lead to the blue-emitting state, $^2H_{9/2}$, or by back energy transfer to Yb^{3+} ions to red emitting $^4F_{9/2}$.[6] The long rise and decay time of the $^4F_{9/2} \rightarrow {}^4I_{15/2}$ transition are explained by the fact that the $^4S_{3/2}$ and $^2H_{11/2}$ states are the initial states for the energy transfer from Yb^{3+} ions, leading to excitation of the Er^{3+} ions to their $^4G/^2K$ states.[6]

The $^2H_{9/2} \rightarrow {}^4I_{15/2}$ transition must be preceded by three-photon absorption. The third photon may be absorbed by Er^{3+}

DOI: 10.1021/acs.inorgchem.8b00484
Inorg. Chem. XXXX, XXX, XXX−XXX

ions in their $^4F_{9/2}$ excited state achieved by two pathways mentioned above. However, absorption from the $^2H_{11/2}$ excited state is also possible, as mentioned above. Both possible mechanisms lead to the emission of blue light.

CONCLUSIONS

Alkaline, M^{2+}, and rare earth, RE^{3+}, fluorides as well as their Yb^{3+}/Er^{3+}-doped counterparts were synthesized by the hydrothermal method. Three different M^{2+} ions, Ca^{2+}, Sr^{2+} and Ba^{2+}, and four RE^{3+} ions, Y^{3+}, La^{3+}, Gd^{3+}, and $Lu^{3,}$ were used in order to obtain upconverting materials. The synthesized compounds crystallized with $M_{0.67}RE_{0.33}F_{2.33}$ composition in a cubic crystal cell. The mechanism of material formation was studied, indicating the influence of the stability of the metal ion EDTA complexes on the final product composition. The tendency to getting lower than expected concentrations of RE^{3+} metal ions forming complexes with EDTA of high stability was observed. Comparison of the XRD patterns to the references confirmed the formation of nanocrystals of cubic structure. Nanocrystal sizes determined from XRD patterns were in the range of 10−21 nm. Similar results were obtained by analyzing TEM images, which revealed sizes in the range of 9−37 nm.

All of the Yb^{3+}- and Er^{3+}-doped materials exhibited UC phenomenon. The most intense emission under 976 nm excitation was observed for Sr_2LuF_7:Yb^{3+},Er^{3+}, Ba_2LuF_7:Yb^{3+},Er^{3+}, and Ba_2GdF_7:Yb^{3+},Er^{3+} samples. Luminescence lifetimes were in the range of 7.5−521 μs, depending on the sample, and indicating the complexity of the obtained systems and energy processes occurred. Energy transfer between Yb^{3+} and Er^{3+} ions was also analyzed by measuring the dependence of the integral luminescence intensity on the excitation laser energy. Analysis of experimental data revealed the occurrence of the two- and three-photon processes, preceding the observed upconversion luminescence. In addition, the presence of quenching phenomena was noticed.

The UCQY measured for the two the best emitting samples Sr_2LuF_7:Yb^{3+},Er^{3+}, Ba_2LuF_7:Yb^{3+},Er^{3+} (0.0192 ± 0.001% and 0.0176 ± 0.001% respectively) prove good properties of used fluoride compounds as hosts for upconverting Yb^{3+} and Er^{3+} ions. The obtained values were similar to those reported for $NaYF_4$ and $NaGdF_4$, known as the best hosts for UC applications.[36,44,67,99,100] This result proves the effectiveness of the hydrothermal method which is also easier and more ecofriendly than the thermal decomposition method, as the synthesis conditions do not require inert atmosphere or a vacuum as well as organic solvents. The hydrothermal method may be considered as a good alternative and complementary method for the synthesis of UCNPs.

This study has also shown the importance of such factors as the stability of the precursors in the hydrothermal conditions and the difference between the ionic radii of metal ions forming the host compound, on the spectroscopic properties of the final product. In addition, the necessity of composition determination by a highly accurate technique (ICP-OES) was emphasized. From the series of studied materials, the most promising for further research and applications are Sr_2LuF_7:Yb^{3+},Er^{3+} and Ba_2LuF_7:Yb^{3+},Er^{3+}. They can be obtained in hydrothermal conditions as nanomaterials with minimal risk of lower than expected concentrations of Yb^{3+} and Er^{3+} dopant ions.

ASSOCIATED CONTENT

Supporting Information

The Supporting Information is available free of charge on the ACS Publications website at DOI: 10.1021/acs.inorgchem.8b00484.

Table S1: Solubility of metal ions fluorides and stability constants of M^{2+} and RE^{3+} complexes with EDTA; Table S2: Upconversion quantum yields of noncore/shell nanoparticles with similar size to the described in the article products; Figure S1: Schematic representation of system setup used to measure upconversion quantum yields; Figure S2: Integral emission intensities of the red and the green bands, and the ratio between them calculated for the obtained samples; Figure S3: Upconversion luminescence decays; Figure S4: Comparison of upconversion luminescence dependencies on laser energy) (PDF)

AUTHOR INFORMATION

Corresponding Author

*E-mail: tgrzyb@amu.edu.pl.

ORCID

Tomasz Grzyb: 0000-0002-2947-6366

Notes

The authors declare no competing financial interest.

ACKNOWLEDGMENTS

Funding for this research was provided by the National Science Centre, Poland (Grant No. DEC-2011/03/D/ST5/05701 and DEC-2016/22/E/ST5/00016).

REFERENCES

(1) Chuai, X.; Guo, X.; Liu, X.; He, G.; Zheng, K.; He, C.; Qin, W. Bifunctional $NaGdF_4$:Yb,Er,Fe Nanocrystals with the Enhanced Upconversion Fluorescence. *Opt. Mater.* **2015**, *44*, 13−17.

(2) Zhang, Y.; Liu, X.; Lang, Y.; Yuan, Z.; Zhao, D.; Qin, G.; Qin, W. Synthesis of Ultra-Small $BaLuF_5$:Yb^{3+},Er^{3+} @$BaLuF_5$:Yb^{3+} Active-Core−active-Shell Nanoparticles with Enhanced. *J. Mater. Chem. C* **2015**, *3*, 2045−2053.

(3) Rao, L.; Lu, W.; Zeng, T.; Yi, Z.; Wang, H.; Liu, H.; Zeng, S. One-Pot Synthesis of PEG Modified $BaLuF_5$:Gd/Yb/Er Nanoprobes for Dual-Modal in Vivo Upconversion Luminescence and X-Ray Bioimaging. *Dalton Trans.* **2014**, *43*, 13343−13348.

(4) Dong, H.; Sun, L.-D.; Yan, C.-H. Energy Transfer in Lanthanide Upconversion Studies for Extended Optical Applications. *Chem. Soc. Rev.* **2015**, *44*, 1608−1634.

(5) Liu, G. Advances in the Theoretical Understanding of Photon Upconversion in Rare-Earth Activated Nanophosphors. *Chem. Soc. Rev.* **2015**, *44*, 1635−1652.

(6) Berry, M. T.; May, P. S. Disputed Mechanism for NIR-to-Red Upconversion Luminescence in $NaYF_4$:Yb^{3+},Er^{3+}. *J. Phys. Chem. A* **2015**, *119*, 9805−9811.

(7) Li, X.; Gai, S.; Li, C.; Wang, D.; Niu, N.; He, F.; Yang, P. Monodisperse Lanthanide Fluoride Nanocrystals: Synthesis and Luminescent Properties. *Inorg. Chem.* **2012**, *51*, 3963−3971.

(8) Wang, F.; Banerjee, D.; Liu, Y.; Chen, X.; Liu, X. Upconversion Nanoparticles in Biological Labeling, Imaging, and Therapy. *Analyst* **2010**, *135*, 1839−1854.

(9) Auzel, F. Compteur Quantique Par Transfert D'energie Entre de Yb^{3+} a Tm^{3+} Dans Un Tungstate Mixte et Dans Verre Germanate. *C. R. Acad. Sci. Paris B* **1966**, *263*, 819−821.

(10) Auzel, F. Upconversion and Anti-Stokes Processes with f and d Ions in Solids. *Chem. Rev.* **2004**, *104*, 139−173.

DOI: 10.1021/acs.inorgchem.8b00484
Inorg. Chem. XXXX, XXX, XXX−XXX

(11) Brites, C. D. S.; Millán, A.; Carlos, L. D. Lanthanides in Luminescent Thermometry. In *Handbook on the Physics and Chemistry of Rare Earths*; Bünzli, J.-C., Pecharsky, V., Eds.; Elsevier, 2016; Vol. *49*, pp 339−427.
(12) Chen, G.; Qiu, H.; Prasad, P. N.; Chen, X. Upconversion Nanoparticles: Design, Nanochemistry, and Applications in Theranostics. *Chem. Rev.* **2014**, *114*, 5161−5214.
(13) DaCosta, M. V.; Doughan, S.; Han, Y.; Krull, U. J. Lanthanide Upconversion Nanoparticles and Applications in Bioassays and Bioimaging: A Review. *Anal. Chim. Acta* **2014**, *832*, 1−33.
(14) Smet, P. F.; Van den Eeckhout, K.; De Clercq, O. Q.; Poelman, D. *Persistent Phosphors*; 1st ed.; Elsevier B.V., 2015; Vol. *48*.
(15) Reszczyńska, J.; Grzyb, T.; Wei, Z.; Klein, M.; Kowalska, E.; Ohtani, B.; Zaleska-Medynska, A. Photocatalytic Activity and Luminescence Properties of RE^{3+}−TiO_2 Nanocrystals Prepared by Sol−gel and Hydrothermal Methods. *Appl. Catal., B* **2016**, *181*, 825−837.
(16) van der Ende, B. M.; Aarts, L.; Meijerink, A. Lanthanide Ions as Spectral Converters for Solar Cells. *Phys. Chem. Chem. Phys.* **2009**, *11*, 11081−11095.
(17) Yang, D.; Dai, Y.; Liu, J.; Zhou, Y.; Chen, Y.; Li, C.; Ma, P.; Lin, J. Ultra-Small $BaGdF_5$-Based Upconversion Nanoparticles as Drug Carriers and Multimodal Imaging Probes. *Biomaterials* **2014**, *35*, 2011−2023.
(18) Feng, L.; Gai, S.; He, F.; Dai, Y.; Zhong, C.; Yang, P.; Lin, J. Multifunctional Mesoporous ZrO_2 encapsulated Upconversion Nanoparticles for Mild NIR Light Activated Synergistic Cancer Therapy. *Biomaterials* **2017**, *147*, 39−52.
(19) Xu, J.; Gulzar, A.; Liu, Y.; Bi, H.; Gai, S.; Liu, B.; Yang, D.; He, F.; Yang, P. Integration of IR-808 Sensitized Upconversion Nanostructure and MoS_2 Nanosheet for 808 Nm NIR Light Triggered Phototherapy and Bioimaging. *Small* **2017**, *13*, 1701841.
(20) Xu, J.; Yang, P.; Sun, M.; Bi, H.; Liu, B.; Yang, D.; Gai, S.; He, F.; Lin, J. Highly Emissive Dye-Sensitized Upconversion Nanostructure for Dual-Photosensitizer Photodynamic Therapy and Bioimaging. *ACS Nano* **2017**, *11*, 4133−4144.
(21) Cheng, Z.; Lin, J. Synthesis and Application of Nanohybrids Based on Upconverting Nanoparticles and Polymers. *Macromol. Rapid Commun.* **2015**, *36*, 790−827.
(22) Chen, D. Q.; Yu, Y. L.; Huang, F.; Lin, H.; Huang, P.; Yang, a P.; Wang, Z. X.; Wang, Y. S. Lanthanide Dopant-Induced Formation of Uniform Sub-10 Nm Active-Core/active-Shell Nanocrystals with near-Infrared to near-Infrared Dual-Modal Luminescence. *J. Mater. Chem.* **2012**, *22*, 2632−2640.
(23) Wang, C.; Cheng, L.; Liu, Z. Upconversion Nanoparticles for Photodynamic Therapy and Other Cancer Therapeutics. *Theranostics* **2013**, *3*, 317−330.
(24) Villa, I.; Vedda, A.; Cantarelli, I. X.; Pedroni, M.; Piccinelli, F.; Bettinelli, M.; Speghini, A.; Quintanilla, M.; Vetrone, F.; Rocha, U.; Jacinto, C.; Carrasco, E.; Rodríguez, F.; Juarranz, A.; del Rosal, B.; Ortgies, D. H.; Gonzalez, P. H.; Solé, J. G.; Garcia, D. J. 1.3 Mm Emitting SrF_2:Nd^{3+} Nanoparticles for High Contrast in Vivo Imaging in the Second Biological Window. *Nano Res.* **2015**, *8*, 649−665.
(25) Runowski, M.; Ekner-Grzyb, A.; Mrówczyńska, L.; Balabhadra, S.; Grzyb, T.; Paczesny, J.; Zep, A.; Lis, S. Synthesis and Organic Surface Modification of Luminescent, Lanthanide-Doped Core/Shell Nanomaterials (LnF_3@SiO_2@NH_2@Organic Acid) for Potential Bioapplications: Spectroscopic, Structural, and in Vitro Cytotoxicity Evaluation. *Langmuir* **2014**, *30*, 9533−9543.
(26) Dou, Q. Q.; Guo, H. C.; Ye, E. Near-Infrared Upconversion Nanoparticles for Bio-Applications. *Mater. Sci. Eng., C* **2014**, *45*, 635−643.
(27) Grzyb, T.; Runowski, M.; Dąbrowska, K.; Giersig, M.; Lis, S. Structural, Spectroscopic and Cytotoxicity Studies of TbF_3@CeF_3 and TbF_3@CeF_3@SiO_2 Nanocrystals. *J. Nanopart. Res.* **2013**, *15*, 1958.
(28) Runowski, M.; Goderski, S.; Paczesny, J.; Księżopolska-Gocalska, M.; Ekner-Grzyb, A.; Grzyb, T.; Rybka, J. D.; Giersig, M.; Lis, S. Preparation of Biocompatible, Luminescent-Plasmonic Core/Shell Nanomaterials Based on Lanthanide and Gold Nanoparticles Exhibiting SERS Effects. *J. Phys. Chem. C* **2016**, *120*, 23788−23798.
(29) Chen, J.; Zhao, J. X. Upconversion Nanomaterials: Synthesis, Mechanism, and Applications in Sensing. *Sensors* **2012**, *12*, 2414−2435.
(30) Muhr, V.; Wilhelm, S.; Hirsch, T.; Wolfbeis, O. S. Upconversion Nanoparticles: From Hydrophobic to Hydrophilic Surfaces. *Acc. Chem. Res.* **2014**, *47*, 3481−3493.
(31) Sperling, R. a; Parak, W. J. Surface Modification, Functionalization and Bioconjugation of Colloidal Inorganic Nanoparticles. *Philos. Trans. R. Soc., A* **2010**, *368*, 1333−1383.
(32) Gnach, A.; Lipinski, T.; Bednarkiewicz, A.; Rybka, J.; Capobianco, J. a. Upconverting Nanoparticles: Assessing the Toxicity. *Chem. Soc. Rev.* **2015**, *44*, 1561−1584.
(33) De, G.; Qin, W.; Wang, W.; Gui, B. Infrared-to-Ultraviolet Upconversion Luminescence of $La_{0.95}Yb_{0.49}Tm_{0.01}F_3$ Nanostructures. *Opt. Commun.* **2009**, *282*, 2950−2953.
(34) Xu, C.; Ma, M.; Yang, L.; Zeng, S.; Yang, Q. Upconversion Luminescence and Magnetic Properties of Ligand-Free Monodisperse Lanthanide Doped $BaGdF_5$ Nanocrystals. *J. Lumin.* **2011**, *131*, 2544−2549.
(35) Jiang, T.; Qin, W.; Di, W.; Yang, R.; Liu, D.; Zhai, X.; Qin, G. Citric Acid-Assisted Hydrothermal Synthesis of α-$NaYF_4$:Yb^{3+},Tm^{3+} Nanocrystals and Their Enhanced Ultraviolet Upconversion Emissions. *CrystEngComm* **2012**, *14*, 2302.
(36) Brites, C. D. S.; Xie, X.; Debasu, M. L.; Qin, X.; Chen, R.; Huang, W.; Rocha, J.; Liu, X.; Carlos, L. D. Instantaneous Ballistic Velocity of Suspended Brownian Nanocrystals Measured by Upconversion Nanothermometry. *Nat. Nanotechnol.* **2016**, *11*, 851.
(37) Voß, B.; Nordmann, J.; Uhl, A.; Komban, R.; Haase, M. Effect of the Crystal Structure of Small Precursor Particles on the Growth of β-$NaREF_4$ (RE = Sm, Eu, Gd, Tb) Nanocrystals. *Nanoscale* **2013**, *5*, 806−812.
(38) Yan, C.-H.; Yan, Z.-G.; Du, Y.-P.; Shen, J.; Zhang, C.; Feng, W. Controlled Synthesis and Properties of Rare Earth Nanomaterials. In *Handbook on the Physics and Chemistry of Rare Earths*; Gschneidner, K. A., Bünzli, J.-C., Pecharsky, V., Eds.; Elsevier, 2011; Vol. *41*, pp 275−472.
(39) Fedorov, P. P.; Luginina, A. A.; Ermakova, J. A.; Kuznetsov, S. V.; Voronov, V. V.; Uvarov, O. V.; Pynenkov, A. A.; Nishchev, K. N. Preparation of Nanodispersed Fluorite-Type $Sr_{1-x}R_xF_{2+x}$ (R = Er, Yb, Ho) Phases from Citrate Solutions. *J. Fluorine Chem.* **2017**, *194*, 8−15.
(40) Grzyb, T.; Runowski, M.; Szczeszak, A.; Lis, S. Influence of Matrix on the Luminescent and Structural Properties of Glycerine-Capped, Tb^{3+} -Doped Fluoride Nanocrystals. *J. Phys. Chem. C* **2012**, *116*, 17188−17196.
(41) Mayakova, M. N.; Luginina, A. A.; Kuznetsov, S. V.; Voronov, V. V.; Ermakov, R. P.; Baranchikov, A. E.; Ivanov, V. K.; Karban, O. V.; Fedorov, P. P. Synthesis of SrF_2-YF_3 nanopowders by Co-Precipitation from Aqueous Solutions. *Mendeleev Commun.* **2014**, *24*, 360−362.
(42) Shi, F.; Zhao, Y. Sub-10 Nm and Monodisperse β-$NaYF_4$:Yb,Tm,Gd Nanocrystals with Intense Ultraviolet Upconversion Luminescence. *J. Mater. Chem. C* **2014**, *2*, 2198−2203.
(43) Kaiser, M.; Würth, C.; Kraft, M.; Hyppänen, I.; Soukka, T.; Resch-Genger, U. Power-Dependent Upconversion Quantum Yield of $NaYF_4$:Yb^{3+},Er^{3+} Nano- and Micrometer-Sized Particles − Measurements and Simulations. *Nanoscale* **2017**, *9*, 10051−10058.
(44) Boyer, J.-C.; van Veggel, F. C. J. M. Absolute Quantum Yield Measurements of Colloidal $NaYF_4$: Er^{3+}, Yb^{3+} Upconverting Nanoparticles. *Nanoscale* **2010**, *2*, 1417.
(45) Nadort, A.; Sreenivasan, V. K. A.; Song, Z.; Grebenik, E. A.; Nechaev, A. V.; Semchishen, V. A.; Panchenko, V. Y.; Zvyagin, A. V. Quantitative Imaging of Single Upconversion Nanoparticles in Biological Tissue. *PLoS One* **2013**, *8*, e63292.
(46) Würth, C.; Kaiser, M.; Wilhelm, S.; Grauel, B.; Hirsch, T.; Resch-Genger, U. Excitation Power Dependent Population Pathways and Absolute Quantum Yields of Upconversion Nanoparticles in Different Solvents. *Nanoscale* **2017**, *9*, 4283−4294.

DOI: 10.1021/acs.inorgchem.8b00484
Inorg. Chem. XXXX, XXX, XXX−XXX

(47) Mao, Y.; Ma, M.; Gong, L.; Xu, C.; Ren, G.; Yang, Q. Controllable Synthesis and Upconversion Emission of Ultrasmall near-Monodisperse Lanthanide-Doped Sr_2LaF_7 Nanocrystals. *J. Alloys Compd.* **2014**, *609*, 262−267.
(48) Liu, Q.; Yan, X.; Chen, Y.; Wang, X. Upconversion Emission of $SrYbF_5$:Er^{3+} Nanosheets Modified by Tm^{3+} Ions. *J. Rare Earths* **2013**, *31*, 1053−1058.
(49) Ma, M.; Xu, C.; Yang, L.; Yang, Q.; Lin, J. Solvothermal Synthesis and Tailored Upconversion Emission of Monodisperse Ultrasmall Face-Centered Cubic Sr_2YF_7 Nanocrystals. *J. Alloys Compd.* **2012**, *525*, 97−102.
(50) Guo, L.; Wang, Y.; Zhang, J.; Dong, P.; Wang, Y. Crystal Structure and up- and down-Conversion Properties of Yb^{3+}, Ho^{3+} Codoped $BaGdF_5$ Solid-Solution with Different Morphologies. *CrystEngComm* **2012**, *14*, 3131.
(51) Du, H.; Zhang, W.; Sun, J. Structure and Upconversion Luminescence Properties of $BaYF_5$:Yb^{3+},Er^{3+} Nanoparticles Prepared by Different Methods. *J. Alloys Compd.* **2011**, *509*, 3413−3418.
(52) Chen, C.; Liu, J.; Chen, Y.; Li, C.; Liu, X.; Huang, H.; Liang, C.; Lou, Y.; Shi, Z.; Feng, S. Sub-10 Nm Sr_2LuF_7:Yb/Er@Sr_2 GdF_7@SrF_2 Up-Conversion Nanocrystals for Up-Conversion Luminescence−Magnetic Resonance−Computed Tomography Trimodal Bioimaging. *ACS Appl. Mater. Interfaces* **2017**, *9*, 5748−5756.
(53) Gong, L.; Ma, M.; Xu, C.; Li, X.; Wang, S.; Lin, J.; Yang, Q. Multicolor Upconversion Emission of Dispersed Ultrasmall Cubic Sr_2LuF_7 Nanocrystals Synthesized by a Solvothermal Process. *J. Lumin.* **2013**, *134*, 718−723.
(54) Chuai, X.; Zhang, D.; Zhao, D.; Zheng, K.; He, C.; Shi, F.; Wang, L.; Chen, H.; Qin, W. Synthesis and Characterization of Yb^{3+},Tm^{3+}:Ba_2YF_7 Nanocrystalline with Efficient Upconversion Fluorescence. *Mater. Lett.* **2011**, *65*, 2368−2370.
(55) Chuai, X.; Yin, F.; Liu, Z.; Shi, F.; Wang, J.; Wang, L.; Zheng, K.; He, C.; Qin, W. Tunable Upconversion Emission in Ba_2YF_7:Yb^{3+}/Er^{3+} Nanocrystals with Different Yb^{3+} Concentration. *Mater. Res. Bull.* **2013**, *48*, 2361−2364.
(56) Li, H.; Liu, G.; Wang, J.; Dong, X.; Yu, W. Hydrothermal Synthesis, down-/enhanced up-Converting, Color Tuning Luminescence, Energy Transfer and Paramagnetic Properties of Ln^{3+} (Ln = Eu/Dy, Yb/Ho)-Doped Ba_2GdF_7 Multifunctional Nanophosphors. *New J. Chem.* **2017**, *41*, 1609−1617.
(57) Greis, O.; Haschke, J. M. Chapter 45: Rare Earth Fluorides. *Handbook on the Physics and Chemistry of Rare Earths* **1982**, *5*, 387−460.
(58) Golubev, A. M.; Simonov, V. I. Superlattice Structures Based on Fluorite. *Kristallografiya* **1986**, *31*, 478.
(59) Sobolev, B. P. Part 1. The High Temperature Chemistry of the Rare Earth Trifluorides. In *The Rare Earth Trifluorides*; Institut dÈstudis Catalans: Barcelona, 2000; p 520.
(60) Fedorov, P. P.; Mayakova, M. N.; Kuznetsov, S. V.; Voronov, V. V.; Ermakov, R. P.; Samarina, K. S.; Popov, A. I.; Osiko, V. V. Co-Precipitation of Yttrium and Barium Fluorides from Aqueous Solutions. *Mater. Res. Bull.* **2012**, *47*, 1794−1799.
(61) Sun, J.; Xian, J.; Du, H. Hydrothermal Synthesis of $BaYF_5$:Yb^{3+}/Er^{3+} Upconversion Luminescence Submicrospheres by a Surfactant-Free Aqueous Solution Route. *J. Phys. Chem. Solids* **2011**, *72*, 207−213.
(62) Yan, Z.-Y.; Yan, B. Luminescent Hybrid Ionogels Functionalized with Rare Earth Fluoride up-Conversion Nanocrystals Dispersing in Ionic Liquid. *Photochem. Photobiol.* **2013**, *89*, 1262−1268.
(63) Huang, S.; Gao, Q.; Gu, M. Enhanced Luminescence in Transparent Glass Ceramics Containing $BaYF_5$: Ce^{3+} Nanocrystals. *J. Lumin.* **2012**, *132*, 750−754.
(64) Lutterotti, L.; Bortolotti, M. Object Oriented Programming and Fast Computation Techniques in Maud, a Program for Powder Diffraction Analysis Written in Java. *Compcomm. Newsl.* **2003**, *1*, 43−50.
(65) Wang, J.; Deng, R.; MacDonald, M. A.; Chen, B.; Yuan, J.; Wang, F.; Chi, D.; Hor, T. S. A.; Zhang, P.; Liu, G.; Han, Y.; Liu, X. Enhancing Multiphoton Upconversion through Energy Clustering at Sublattice Level. *Nat. Mater.* **2014**, *13*, 157−162.
(66) Balabhadra, S.; Debasu, M. L.; Brites, C. D. S.; Ferreira, R. A. S.; Carlos, L. D. A Cost-Effective Quantum Yield Measurement Setup for Upconverting Nanoparticles. *J. Lumin.* **2017**, *189*, 64−70.
(67) Li, X.; Shen, D.; Yang, J.; Yao, C.; Che, R.; Zhang, F.; Zhao, D. Successive Layer-by-Layer Strategy for Multi-Shell Epitaxial Growth: Shell Thickness and Doping Position Dependence in Upconverting Optical Properties. *Chem. Mater.* **2013**, *25*, 106−112.
(68) Wang, G.; Peng, Q.; Li, Y. Synthesis and Upconversion Luminescence of BaY_2F_8:Yb^{3+}/Er^{3+} Nanobelts. *Chem. Commun.* **2010**, *46*, 7528−7529.
(69) Xingren, L.; Gang, X.; Powell, R. C. Fluorescence and Energy-Transfer Characteristics of Rare Earth Ions in $BaYF_5$ Crystals. *J. Solid State Chem.* **1986**, *62*, 83−91.
(70) Sobolev, B. P.; Golubev, A. M.; Otroshchenko, L. P.; Molchanov, V. N.; Zakalyukin, R. M.; Ryzhova, E. A.; Herrero, P. $Ba_{1-x}R_xF_{2+x}$ Phases (R = Gd-Lu) with Distorted Fluorite-Type Structures—products of Crystallization of Incongruent Melts in the BaF_2-RF_3 Systems (R = Gd-Lu). III. Defect $Ba_{0.75}Lu_{0.25}F_{2.25}$ Structure. A New $\{Lu_8[Ba_6F_{71}]\}$ Supercluster of Defects. *Crystallogr. Rep.* **2003**, *48*, 944−952.
(71) Sorokin, N. I.; Karimov, D. N.; Sul'yanova, E. A.; Sobolev, B. P. Nanostructured Crystals of Fluorite Phases $Sr_{1-x}R_xF_{2+x}$ and Their Ordering: 12. Influence of Structural Ordering on the Fluorine-Ion Conductivity of $Sr_{0.667}R_{0.333}F_{2.333}$ Alloys (R = Tb or Tm) at Their Annealing. *Crystallogr. Rep.* **2018**, *63*, 121−126.
(72) Greis, O.; Cader, M. S. R. Preparation and Characterization of Fluorite-Related Superstructure Phases Sr_2RF_7, with R: Sm - Lu and Y. *Chem. Informationsdienst* **1986**, *17*, 1754−1758.
(73) Xiang, L.; Ren, G.; Mao, Y.; He, J.; Su, R. Controllable Synthesis and Upconversion Emission of Ultrasmall Lanthanide-Doped Sr_2GdF_7 Nanocrystals. *Opt. Mater.* **2015**, *49*, 6−14.
(74) Sobolev, B. P.; Golubev, A. M.; Krivandina, E. A.; Marychev, M. O.; Chuprunov, E. V.; Alcobe, X.; Gali, S.; Pascual, L.; Rojas, R.-M.; Herrero, P. $Ba_{1-x}R_xF_{2+x}$ Phases (R = Gd-Lu) with Distorted Fluorite-Type Structure— Products of Crystallization of Incongruent Melts in the BaF_2-RF_3 Systems. I. $Ba_{0.75}$ $R_{0.25}F_{2.25}$ Crystals (Synthesis and Some Characteristics). *Crystallogr. Rep.* **2002**, *47*, 201−212.
(75) Rosenthal, S. J.; McBride, J.; Pennycook, S. J.; Feldman, L. C. Synthesis, Surface Studies, Composition and Structural Characterization of CdSe, Core/shell and Biologically Active Nanocrystals. *Surf. Sci. Rep.* **2007**, *62*, 111−157.
(76) Shannon, R. D. Revised Effective Ionic Radii and Systematic Studies of Interatomie Distances in Halides and Chaleogenides. *Acta Crystallogr., Sect. A: Cryst. Phys., Diffr., Theor. Gen. Crystallogr.* **1976**, *32*, 751−767.
(77) *CRC Handbook of Chemistry and Physics*, 84th ed.; Lide, D. R., Ed.; CRC Press, 2004.
(78) Menon, M. P.; James, J. Solubilities, Solubility Products and Solution Chemistry of Lanthanon Trifluoride-Water Systems. *J. Chem. Soc., Faraday Trans. 1* **1989**, *85*, 2683.
(79) *The Rare Earths in Modern Science and Technology*; McCarthy, G. J.; Rhyne, J. J.; Silber, H. B., Eds.; Springer US: Boston, MA, 1980; Vol. 2.
(80) Martell, A. E.; Motekaitis, R. J.; Fried, A. R.; Wilson, J. S.; MacMillan, D. T. Thermal Decomposition of EDTA, NTA, and Nitrilotrimethylenephosphonic Acid in Aqueous Solution. *Can. J. Chem.* **1975**, *53*, 3471−3476.
(81) Scherrer, P. Bestimmung Der Grösse Und Der Inneren Struktur von Kolloidteilchen Mittels Röntgenstrahlen. *Nachr. Ges. Wiss. Göttingen* **1918**, *26*, 98−100.
(82) Grzyb, T.; Balabhadra, S.; Przybylska, D.; Węcławiak, M. Upconversion Luminescence in $BaYF_5$, $BaGdF_5$ and $BaLuF_5$ Nanocrystals Doped with Yb^{3+}/Ho^{3+}, Yb^{3+}/Er^{3+} or Yb^{3+}/Tm^{3+} Ions. *J. Alloys Compd.* **2015**, *649*, 606−616.
(83) Page, R. H.; Schaffers, K. I.; Waide, P. A.; Tassano, J. B.; Payne, S. A.; Krupke, W. F.; Bischel, W. K. Upconversion-Pumped

DOI: 10.1021/acs.inorgchem.8b00484
Inorg. Chem. XXXX, XXX, XXX−XXX

Luminescence Efficiency of Rare-Earth-Doped Hosts Sensitized with Trivalent Ytterbium. *J. Opt. Soc. Am. B* **1998**, *15*, 996.
(84) Fischer, S.; Johnson, N. J. J.; Pichaandi, J.; Goldschmidt, J. C.; Van Veggel, F. C. J. M. Upconverting Core-Shell Nanocrystals with High Quantum Yield under Low Irradiance: On the Role of Isotropic and Thick Shells. *J. Appl. Phys.* **2015**, *118*, 193105.
(85) Pokhrel, M.; Gangadharan, A. K.; Sardar, D. K. High Upconversion Quantum Yield at Low Pump Threshold in Er^{3+}/Yb^{3+} Doped La_2O_2S Phosphor. *Mater. Lett.* **2013**, *99*, 86−89.
(86) Chen, G.; Ohulchanskyy, T. Y.; Kachynski, A.; Ågren, H.; Prasad, P. N. Intense Visible and near-Infrared Upconversion Photoluminescence in Colloidal $LiYF_4:Er^{3+}$ Nanocrystals under Excitation at 1490 Nm. *ACS Nano* **2011**, *5*, 4981−4986.
(87) Macdougall, S. K. W.; Ivaturi, A.; Marques-Hueso, J.; Richards, B. S. Measurement Procedure for Absolute Broadband Infrared up-Conversion Photoluminescent Quantum Yields: Correcting for Absorption/re-Emission. *Rev. Sci. Instrum.* **2014**, *85*, 063109.
(88) Wrighton, M. S.; Ginley, D. S.; Morse, D. L. Technique for the Determination of Absolute Emission Quantum Yields of Powdered Samples. *J. Phys. Chem.* **1974**, *78*, 2229−2233.
(89) Huang, P.; Zheng, W.; Zhou, S.; Tu, D.; Chen, Z.; Zhu, H.; Li, R.; Ma, E.; Huang, M.; Chen, X. Lanthanide-Doped $LiLuF_4$ Upconversion Nanoprobes for the Detection of Disease Biomarkers. *Angew. Chem., Int. Ed.* **2014**, *53*, 1252−1257.
(90) Liu, X.; Deng, R.; Zhang, Y.; Wang, Y.; Chang, H.; Huang, L.; Liu, X. Probing the Nature of Upconversion Nanocrystals: Instrumentation Matters. *Chem. Soc. Rev.* **2015**, *44*, 1479−1508.
(91) Liu, H.; Xu, C. T.; Lindgren, D.; Xie, H.; Thomas, D.; Gundlach, C.; Andersson-Engels, S. Balancing Power Density Based Quantum Yield Characterization of Upconverting Nanoparticles for Arbitrary Excitation Intensities. *Nanoscale* **2013**, *5*, 4770.
(92) Beeby, A.; Clarkson, I. M.; Dickins, R. S.; Faulkner, S.; Parker, D.; Royle, L.; de Sousa, A. S.; Williams, J. a. G.; Woods, M. Non-Radiative Deactivation of the Excited States of Europium, Terbium and Ytterbium Complexes by Proximate Energy-Matched OH, NH and CH Oscillators: An Improved Luminescence Method for Establishing Solution Hydration States. *J. Chem. Soc., Perkin Trans. 2* **1999**, *2*, 493−504.
(93) Pedroni, M.; Piccinelli, F.; Passuello, T.; Polizzi, S.; Ueda, J.; Haro-González, P.; Martinez Maestro, L.; Jaque, D.; García-Solé, J.; Bettinelli, M.; Speghini, A. Water (H_2O and D_2O) Dispersible NIR-to-NIR Upconverting Yb^{3+}/Tm^{3+} Doped MF_2 (M = Ca, Sr) Colloids: Influence of the Host Crystal. *Cryst. Growth Des.* **2013**, *13*, 4906−4913.
(94) Xiang, G.; Zhang, J.; Hao, Z.; Zhang, X.; Pan, G. H.; Chen, L.; Luo, Y.; Lü, S.; Zhao, H. Solvothermal Synthesis and Upconversion Properties of about 10nm Orthorhombic $LuF_3:Yb^{3+}$, Er^{3+} Rectangular Nanocrystals. *J. Colloid Interface Sci.* **2015**, *459*, 224−229.
(95) Xiang, G.; Zhang, J.; Hao, Z.; Zhang, X.; Luo, Y.; Lü, S.; Zhao, H. Transition to Cubic Phase and Enhancement of Green Upconversion Emission by Adding La^{3+} Ions in Hexagonal $NaLuF_4:Yb^{3+}/Er^{3+}$ Nanocrystals. *CrystEngComm* **2014**, *16*, 2499.
(96) Hu, S.; Wu, X.; Chen, Z.; Hu, P.; Yan, H.; Tang, Z.; Xi, Z.; Liu, Y. Uniform $NaLuF_4$ Nanoparticles with Strong Upconversion Luminescence for Background-Free Imaging of Plant Cells and Ultralow Power Detecting of Trace Organic Dyes. *Mater. Res. Bull.* **2016**, *73*, 6−13.
(97) Grzyb, T.; Gruszeczka, A.; Lis, S. Up-Conversion Luminescence of Yb^{3+} and Er^{3+} Doped YPO_4, $LaPO_4$ and $GdPO_4$ Nanocrystals. *J. Lumin.* **2016**, *175*, 21−27.
(98) Wawrzyńczyk, D. Surface Functionalization of up-Converting $NaYF_4$ Nanocrystals with Chiral Molecules. *RSC Adv.* **2016**, *6*, 5558−5565.
(99) Ostrowski, A. D.; Chan, E. M.; Gargas, D. J.; Katz, E. M.; Han, G.; Schuck, P. J.; Milliron, D. J.; Cohen, B. E. Controlled Synthesis and Single-Particle Imaging of Bright, Sub-10 Nm Lanthanide-Doped Upconverting Nanocrystals. *ACS Nano* **2012**, *6*, 2686−2692.
(100) Wisser, M. D.; Fischer, S.; Maurer, P. C.; Bronstein, N. D.; Chu, S.; Alivisatos, A. P.; Salleo, A.; Dionne, J. A. Enhancing Quantum Yield via Local Symmetry Distortion in Lanthanide-Based Upconverting Nanoparticles. *ACS Photonics* **2016**, *3*, 1523−1530.

DOI: 10.1021/acs.inorgchem.8b00484
Inorg. Chem. XXXX, XXX, XXX−XXX